applied sciences

MDPI

Article

Thermo-Mechanical Behavior of Sandstone and Its Implications for the Stability of Underground Gasification Cavities Under Unloading Conditions

Jiakun Lv [1,2], Bing Chen [2,3,*], Yedan Lu [1], Jian Ma [1], Chengye Yang [4], Jingong Ma [5] and Zhaofei Xu [1]

[1] College of Architecture and Civil Engineering, Jiangsu University of Science and Technology, Zhenjiang 215600, China; 202400000007@just.edu.cn (J.L.)
[2] Institute of Geotechnical and Underground Engineering, Shandong University, Jinan 250000, China
[3] Suzhou Research Institute, Shandong University, Suzhou 215000, China
[4] Sch Engn, Xizang University, Lhasa 850000, China
[5] China Coal Technology & Engineering Group Taiyuan Research Institute Co., Ltd., Taiyuan 030006, China
* Correspondence: cdbakdw@163.com; Tel.: +86-157-6227-3428

Abstract

The extreme thermal environment during the underground coal gasification (UCG) process poses a severe threat to the stability of the gasification cavity and the integrity of the surrounding rock. This paper aims to reveal the thermo-mechanical response characteristics and damage evolution mechanism of sandstone under true triaxial unloading conditions following exposure to high temperatures. Sandstone specimens were thermally pre-treated at five temperature gradients (25 °C, 200 °C, 400 °C, 600 °C, and 800 °C) and subsequently subjected to true triaxial loading and unloading experiments. The effects of varying temperatures on the strength, deformation parameters, dilation angle evolution, and macroscopic failure modes of the sandstone were systematically analyzed. The results indicate a significant critical transition point in the mechanical behavior of the sandstone at 400 °C. Below this threshold, thermal-induced microcrack closure leads to an increase in peak strength (with the peak strength at 800 °C increasing by approximately 67% compared to room temperature). Conversely, above 400 °C, thermal damage to the mineral grains intensifies, causing the crack propagation pattern to transition from brittle shear to a complex tension-shear splitting mode, accompanied by severe dilatancy (with a generalized Poisson's ratio exceeding 0.8). Based on these findings, this study proposes a stage-wise damage evolution model alongside a targeted zonal support strategy, recommending the application of high-prestressed support in high-temperature zones above 400 °C to suppress tensile failure. Ultimately, this research provides a crucial theoretical basis for evaluating the long-term stability of high-temperature underground engineering projects and ensuring operational safety.

Keywords: underground coal gasification; high-temperature sandstone; true triaxial unloading; shear dilatancy; damage evolution; cavity stability

Academic Editor: Luisa F. Cabeza

Received: 15 May 2026
Revised: 9 June 2026
Accepted: 10 June 2026
Published: 12 June 2026

1. Introduction

As mineral resources are explored and developed, there are problems related to the change in rock mechanical properties caused by high temperatures in coal underground gasification, geothermal resources, and deep coal resource mining [1–3]. The physical and mechanical properties, strength characteristics, and microstructures of rocks all change under the influence of temperature, which can seriously affect the long-term stability of underground engineering [4,5]. Compared with other methods of coal mining, the most distinctive feature of coal underground gasification is the production of a temperature of over 600 °C in the gasifier used for the gasification process. Under continuous high temperatures, coal gradually gasifies (forms gas) and produces a combustion void [6–8]. The formation of the combustion void will cause the stress field around the gasifier to be redistributed, specifically with axial loading and radial local unloading [9–12]. It can be concluded from the analysis that the high-temperature environment in the gasifier not only changes the stress field of the surrounding rock but also changes the physical and mechanical properties of the rock. Therefore, conducting research on the mechanical properties changes in high-temperature sandstone under true triaxial stress conditions is of great significance in clarifying the failure mechanism of the surrounding rock under high-temperature conditions, and can also provide important theoretical support for the underground coal gasification process.

Currently, extensive research has been conducted on the physical properties and static mechanical characteristics of rocks under high temperatures and pressures, yielding a plethora of theoretical and applied accomplishments. Gautam et al. [13] discovered that the threshold temperature for the thermal properties of the Jalore granite is 300 °C. Once the temperature surpasses 300 °C, the metamorphism of the granite sample intensifies, resulting in a notable reduction in its thermal conductivity and longitudinal wave velocity. Wan et al. [14–16] carried out conventional triaxial compression experiments on sized granite at high temperatures ranging from 50 to 600 °C and acquired three stages of thermal deformation of granite, along with the critical stress difference between volumetric expansion and volumetric contraction. Liu et al. [17] and Shi et al. [18] conducted in-depth research on the strength and deformation characteristics of sandstone under high temperature and pressure. The results indicate that as the temperature rises, the mechanical properties of rocks, such as compressive strength and modulus of elasticity, exhibit a tendency of initially increasing and subsequently decreasing. Su et al. [19] performed triaxial experiments on marble specimens at various temperatures. The outcomes demonstrated that high temperatures exerted a notable weakening influence on the triaxial compressive strength, elastic modulus, and secant modulus of marble, and had a remarkable impact on its mechanical behavior. Wang et al. [20] carried out an investigation on the strength and mechanical properties of rocks exposed to diverse triaxial stresses subsequent to high-temperature treatment. The findings indicated that the bearing capacity of sandstone exhibited an initial increase followed by a decrease with the ascent of temperature, and the deformation parameters of sandstone were approximately inversely correlated with temperature. Ma et al. [21] simulated the coupling environment of deep rock temperature and stress field, demonstrating that a high temperature of 400 °C is capable of enhancing the strength and modulus of granite. The aforementioned research outcomes systematically examined the physical and mechanical properties of deep rocks under high temperatures from the perspective of high-temperature rock mechanics, establishing a foundation for the research work in high-temperature rock mechanics.

However, the rock mass surrounding underground engineering structures, particularly in deep UCG projects, is rarely subjected to conventional triaxial stress ($\sigma 1 > \sigma 2 = \sigma 3$). Due to tectonic processes and cavity excavation, rocks in geological strata are typically subjected to unequal true triaxial stress in three directions ($\sigma 1 > \sigma 2 > \sigma 3$) [22–24]. Under these conditions, Wei et al. hold the view that the horizontal principal stress significantly affects rock failure processes and strength characteristics, frequently resulting in brittle failure [25,26]. Furthermore, Li et al. [27,28] contend that the internal fracture characteristics of rocks under true triaxial unloading conditions—which closely mimic excavation or void formation—are far more intricate than those under simple loading paths, producing fracture planes with significantly greater surface areas. While these studies underscore the absolute necessity of true triaxial unloading tests to accurately simulate real in situ stress fields, they have predominantly focused on ambient temperature environments, leaving the mechanical response of thermally damaged rocks largely unexplored.

In summary, while the existing literature provides fundamental insights into thermal effects under conventional loading, as well as the behavior of intact rocks under true triaxial unloading, these isolated approaches fail to capture the unique thermo-mechanical environment surrounding underground gasification chambers. The innovation of this work lies in directly bridging this gap: the UCG environment is distinctively characterized by severe high-temperature pre-damage coupled immediately with true triaxial stress relaxation (radial unloading and axial stress accumulation) induced by cavity formation. To address the mechanical response and progressive failure mechanisms under this specific "high-temperature history—stress unloading disturbance," this study systematically investigates the behavior of sandstone. Firstly, the sandstone underwent thermal treatment at diverse temperatures, and subsequently, true triaxial loading and unloading experiments were carried out. Based on the test outcomes, the strength, deformation, and failure characteristics under various temperature circumstances were analyzed. Further studies explored the impact of temperature on deformation parameters and the evolution law of the shear dilatancy angle during unloading. Finally, the shear dilation failure mechanism of sandstone under thermal influence was expounded. These outcomes are highly significant for comprehending the characteristics and laws of sandstone loading and unloading failure under deep high-temperature and high-pressure circumstances, as well as for rationally choosing engineering structural parameters and scientifically assessing rock mass stability.

2. Experimental Procedure

2.1. Sample Preparation

The sandstone used in this study is green sandstone, which is grayish in color and has a hard texture and a dense structure. Its main mineral composition is feldspar and quartz. According to the international rock mechanics test regulations, the large, intact sandstone samples collected on site were cut and processed into 50 mm × 50 mm × 100 mm specimens. The surfaces of the specimens were then polished carefully with a grinding stone to make them smooth and flat, and each pair of opposite surfaces was parallel to each other. The prepared specimens underwent high-temperature pretreatment, and the resultant green sandstone specimens are depicted in Figure 1.

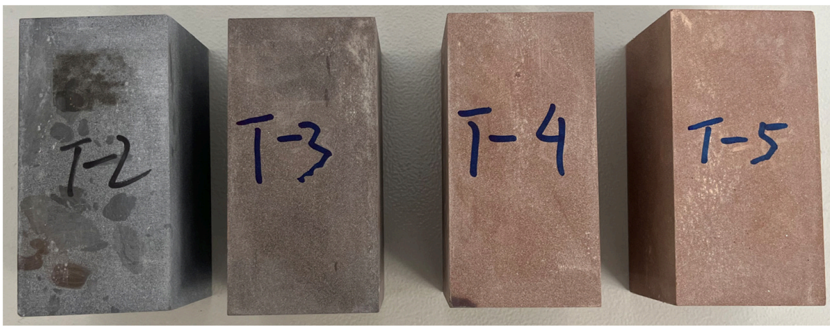

Figure 1. Rock samples after heat treatment.

2.2. True Triaxial Test System

This experiment employed an independently developed rock true triaxial electro-hydraulic servo loading test system, which is primarily composed of a triaxial servo control loading system, a true triaxial pressure cell, and an acoustic emission monitoring system. The triaxial servo-controlled loading system features three independent loading frames, each configured for rigid piston loading.

The σ_1 and σ_3 loading frames are fixedly positioned, while the σ_2 loading frame is placed on a horizontal guide rail, and the true triaxial pressure chamber is precisely located within the piston loading spaces of σ_1, σ_2, and σ_3 through the guide rail.

Figure 2 shows the internal structure diagram of the true triaxial test system with the true triaxial pressure chamber placed on the σ_2 loading frame. In Figure 2, the true triaxial pressure chamber is encompassed by loading blocks arranged in a crosswise pattern, which are respectively linked to the piston rods and counterforce screws in the σ_2 and σ_3 directions. Through adjusting the piston rods and counterforce screws, the sample is precisely placed right below the σ_1 piston rod. The true triaxial pressure chamber incorporates a windmill-shaped loading pad design; prior to testing, a lubricant is applied to the interfaces between the pads and the specimen surface to minimize friction.

The experimental measurements involve standard instrumental uncertainties. The load cells used for axial and lateral stress control in the testing system have a measurement uncertainty of ±0.5% of the full scale. The displacement sensors monitoring axial and radial strains possess an accuracy of ±0.005 mm. Additionally, the temperature controller of the high-temperature muffle furnace maintains a measurement precision of ±2.0 °C.

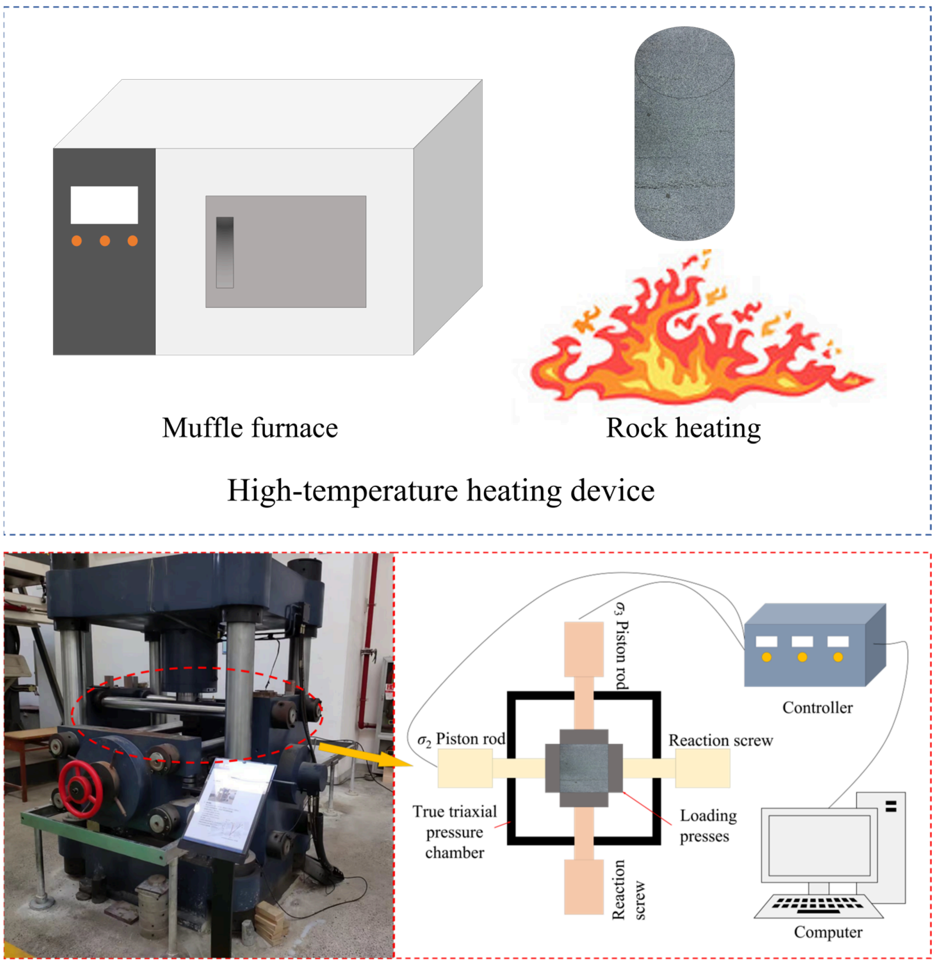

Figure 2. Rock's true triaxial electro-hydraulic loading test system.

2.3. Testing Procedure

The experimental procedure primarily comprises three stages, wherein the true triaxial unloading test is conducted via the method of axial compression paired with lateral confinement unloading (Figure 3).

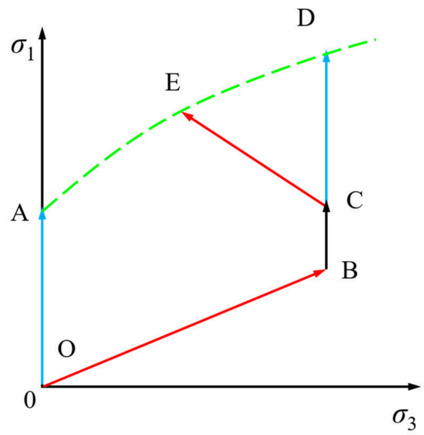

Figure 3. True triaxial unloading path.

(1) High-temperature pretreatment of sandstone specimens

Firstly, the rock sample is subjected to heating within the high-temperature environment of the muffle furnace. The temperature points are set at five grades, namely 25 °C, 200 °C, 400 °C, 600 °C, and 800 °C, with a heating rate of 2 °C/min. To ensure thermal uniformity, each rock specimen is held at the target temperature for 240 min, followed by furnace-cooling to room temperature. The heating duration and the heated specimen are presented in Figure 4.

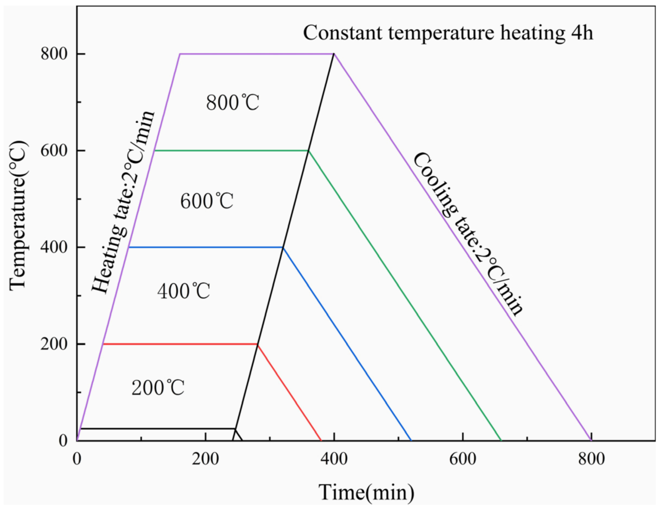

Figure 4. The heat treatment path and morphology of sandstone.

(2) True triaxial loading test

True triaxial compression tests were conducted on sandstone specimens subjected to high-temperature pretreatment. The stress control approach was employed under static water pressure circumstances at a rate of 0.25 MPa/s to impose $\sigma_1 = \sigma_3 = \sigma_2$ upon the initial rock mass (8 MPa) until the overburden pressure was loaded to the preset value. Once the overburden pressure was maintained constant, the stress σ_1 was exerted in the axial direction at a loading rate of 0.25 MPa/s until the green sandstone specimen broke down.

(3) True triaxial unloading failure test

The stress is controlled by the static water pressure condition and increased at a rate of 0.25 MPa/s from $\sigma_1 = \sigma_3 = \sigma_2$ to the initial rock pressure (8 MPa) until the overburden pressure reaches the desired value. Once the confining pressure is loaded to the pre-defined value, maintain the confining pressure at a constant level and augment $\sigma 1$ at a loading rate of 0.25 MPa/s until 80% of the conventional triaxial peak strength of the sandstone is attained. During the unloading of the confining pressure at a rate of 0.05 MPa/s, the axial stress was continuously increased at 0.25 MPa/s until the confining pressure reached 0 MPa. If the specimen remained intact at this point, the axial loading was maintained until macroeconomic failure occurred, which marked the conclusion of the test.

To simulate the quasi-static stress redistribution during underground coal gasification (UCG)—specifically, vertical stress accumulation and radial support loss—synchronized rates of 0.25 MPa/s for axial loading and 0.05 MPa/s for confinement unloading were adopted. This progressive stress path eliminates dynamic impact artifacts, ensuring that the measured variations in deformation modulus and dilatancy angle accurately represent the intrinsic thermo-mechanical behavior of the sandstone.

3. Analysis of the Testing Results

3.1. Stress–Strain Curve Subjected to Temperature Effects

Figure 5 illustrates the complete stress–strain curves of sandstone specimens obtained from both true triaxial loading and confining pressure unloading tests under various thermal conditions. It is observable from the figure that the peak strength of the high-temperature sandstone samples all manifested an increasing tendency along with the rise in the applied temperature. In the course of the true triaxial loading test, the peak strength of the rock sample rose from 90 MPa at ambient temperature to 150 MPa at 800 °C, with an increment of 67%. During the true triaxial confining pressure unloading test, the peak strength of the rock sample climbed from 88 MPa at ambient temperature to 126 MPa at 800 °C, with an increment of 43%. This phenomenon is predominantly attributed to the evaporation of the internal water within the sandstone sample upon high-temperature heating, which induces crystal expansion and the closure of some cracks, thereby reducing the number of cracks and enhancing the compactness of the rock. This subsequently enhances the interlocking of mineral particles within the rock, thereby strengthening its overall mechanical properties.

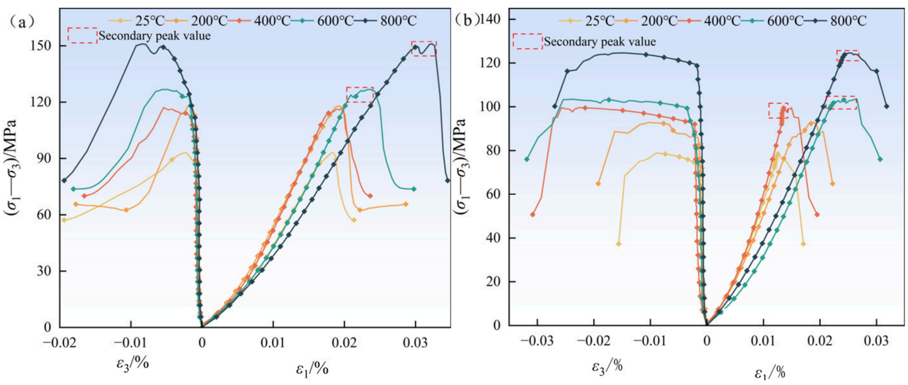

Figure 5. Stress–strain curves under triaxial compression and unloading at different temperatures. (**a**) Triaxial compression; (**b**) Triaxial unloading pressure.

Figure 5b shows the stress–strain curves of sandstone specimens under different temperature conditions during the unloading confining pressure test. It can be observed from the figure that the deformation characteristics are approximately identical before reaching the peak value; however, there are notable differences in the strain within the peak value region. All the sandstone specimens presented a secondary peak phenomenon in the unloading confining pressure curve. Furthermore, as the temperature increased, the sandstone sample exhibited a noticeable degree of ductility, as the internal cracks in the rock sample were able to extend horizontally due to the increased axial pressure and the subsequent release of confining pressure during the axial compression and unloading process. As the axial pressure increased, the cracks became denser again, and the axial stress remained constant due to the interplay of particle forces. It can further be observed from the figure that when the high-temperature rock specimen is deprived of the constraint of confining pressure, its peak strength will also continuously decline. This is in accordance with the research results of Ma et al. [29–31].

3.2. Macro Damage Characteristics of Triaxial Test on High-Temperature Sandstone

Figure 6 shows the macroscopic fracture attributes of sandstone specimens subjected to true triaxial loading and unloading at diverse temperatures. It can be seen from the figure that the macroscopic fracture surface of the sandstone specimen under different temperature conditions during the loading and unloading test process is basically in the shape of a "V" and passes through the entire specimen, which is similar to the results of the true triaxial loading test conducted by Mogi, Haimson, and Feng, etc. [32–35], but the feature of brittle failure of rocks in the unloading path of the true triaxial test is more obvious. By conducting a further analysis of the failure morphology of the sandstone specimens in Figure 6, it becomes apparent that the overall failure pattern of the sandstone specimens under diverse temperature circumstances is fragmentation, accompanied by distinct brittle failure traits. The high-temperature sandstone specimens do not exhibit a tendency for brittle failure to transform into ductile failure. In summary, sandstone specimens underwent brittle failure under true triaxial loading and unloading conditions at different temperatures, and the stress drop to stability was completed in an extremely short time. During the test, the sound of the specimen breaking could be heard when it failed.

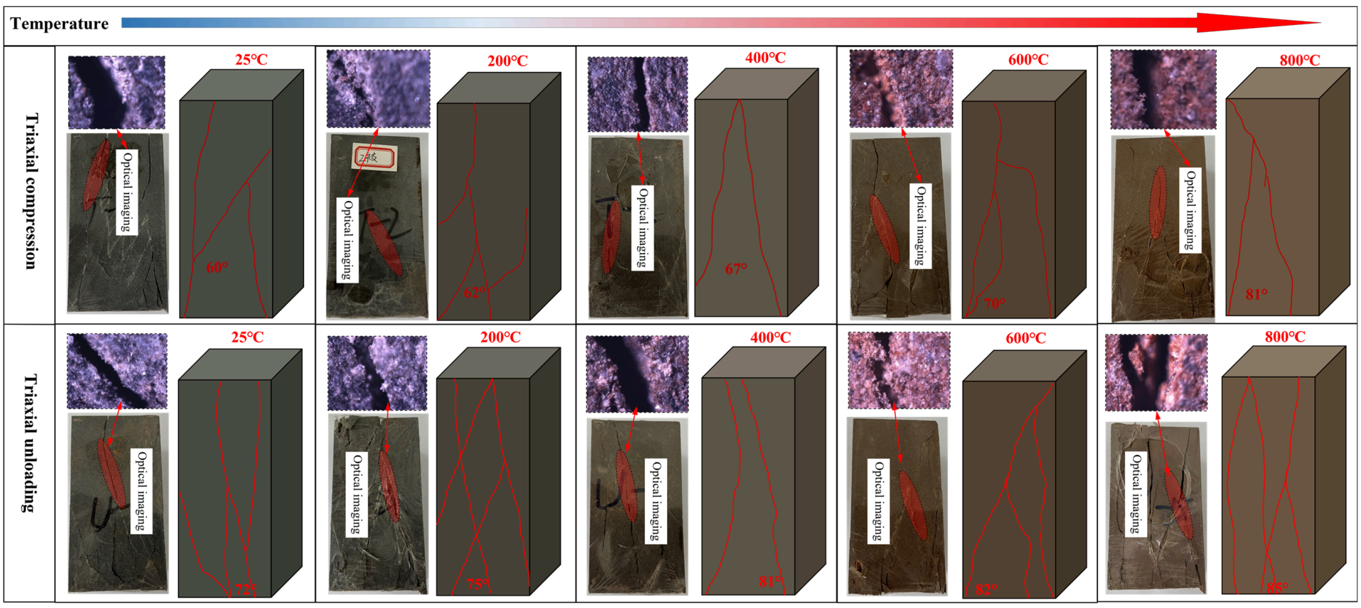

Figure 6. Failure mode diagram of rocks with different temperatures.

It can be seen from the analysis of the failure types of sandstone specimens under different temperature conditions that in the true triaxial loading and unloading tests of sandstone specimens, most of them show typical shear failure. As the initial action temperature increases, the sandstone specimens gradually show the tensile failure mode of layered cleavage destruction. This is due to the fact that high temperatures gave rise to the formation of microcracks within the sandstone sample. Moreover, as the confining pressure was decreased during the unconfined compression test, the microcracks began to evolve under tensile action. Furthermore, we observed the fracture morphology of the sandstone using an optical microscope and found that as the action temperature increased, the fracture surface gradually transitioned from smooth to rough, and the degree of edge fragmentation gradually increased. The specific fracture location is shown in Figure 6. Moreover, as the temperature ascends, local shear failure surfaces are detected on both sides of the macroscopic main failure surface. Concurrently, some shear surfaces possess vertical cracks parallel to the loading direction, which arise from the emergence of vertical forces due to lateral slippage between the failure surfaces during fracture.

In the true triaxial unloading and loading tests, the rock's failure is mainly determined by its internal shear resistance capacity. During the loading phase, owing to the existence of the intermediate principal stress, the sandstone is restricted by the intermediate principal stress to a certain extent, thereby enhancing its ductility to a certain degree and strengthening its capacity to withstand internal shear stress. During the unloading phase, driven by the Poisson effect, significant lateral expansion occurs along the direction of the minimum principal stress, inducing tensile fracturing and rendering the rock highly susceptible to localized failure.

Based on the macroscopic failure characteristics of the sandstone specimens (Figure 6), the variation pattern of the failure angle of the sandstone specimens under different temperature actions is statistically derived and presented in Figure 7. The failure angle refers to the angle between the normal direction of the shear fracture surface and the direction of the maximum principal stress. It can be observed from the data in Figure 7 that the range of the failure angle for the sandstone specimens under different temperature actions lies between 60° and 81°. Moreover, as the temperature of action rises, the failure angle of the sandstone specimens gradually increases, eventually approaching a vertical angle. The angle of failure of the sandstone specimen under unloading failure at the same temperature is also greater than the angle of failure produced by failure under triaxial compression. Based on the results presented in Figures 6 and 7, high temperatures diminish the heterogeneity of sandstone, and the development of cracks during sandstone failure is enhanced.

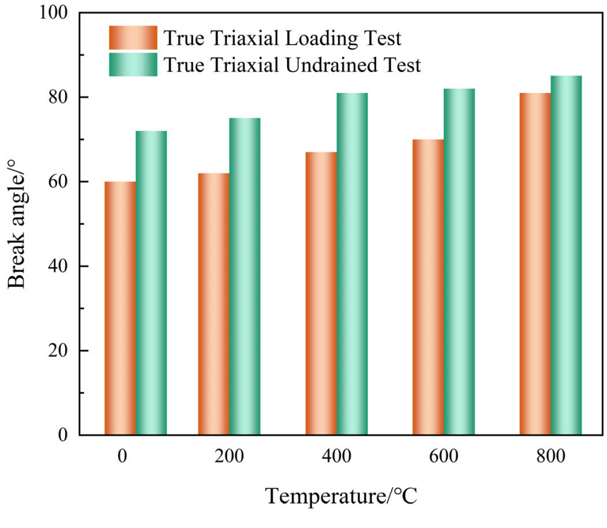

Figure 7. Evolution of the failure angle of rock specimens.

The macroscopic failure and deformation of high-temperature sandstone are strongly governed by applied stress paths and unloading rates. Slower unloading exacerbates time-dependent subcritical crack growth, significantly reducing peak strength and intensifying lateral dilatancy. Concurrently, the coupled path of simultaneous σ_1 loading and σ_3 unloading accelerates deviatoric stress accumulation while releasing lateral constraints. Driven by the Poisson effect, this specific path forces thermally induced microcracks to propagate parallel to σ_1, transitioning the failure mode from conventional localized shear to complex tensile–shear layered cleavage. This profound stress-path dependency highlights the necessity of replicating exact in situ unloading conditions to accurately assess stability and spalling risks in underground gasification cavities.

3.3. Deformation Characteristics

In the previous section, we explored the stress–strain and failure characteristics of sandstone specimens under loading and unloading tests at different temperatures. According to the research findings, the stress evolution path and failure characteristics of high-temperature sandstone specimens in the unloading confining pressure test are more complex, so this section focuses on the deformation characteristics of high-temperature sandstone specimens in the unloading confining pressure test.

The modulus of elasticity E and Poisson's ratio μ are highly significant parameters when we conduct an analysis of the deformation characteristics of high-temperature sandstone specimens under unconfined pressure. For elastic–plastic materials, the deformation modulus will change when the material yields. In addition, Poisson's ratio is usually a constant in the elastic range. To characterize the deformation properties of sandstone under diverse temperature conditions more precisely, this paper refers to the research of Gao et al. [36,37] and introduces the notion of generalized Poisson's ratio (which considers the influences of lateral deformation and temperature) to depict the deformation characteristics during the unloading confining pressure test of high-temperature sandstone. The sandstone specimen satisfies the generalized Hooke's law under high-temperature triaxial stress conditions, as follows:

$$\begin{cases} \varepsilon_1 = [\sigma_1 - \mu_s(\sigma_2 + \sigma_3)]/E_S \\ \varepsilon_2 = [\sigma_2 - \mu_s(\sigma_1 + \sigma_3)]/E_S \\ \varepsilon_3 = [\sigma_3 - \mu_s(\sigma_1 + \sigma_2)]/E_S \end{cases} \tag{1}$$

Under triaxial compression, $\sigma_2 = \sigma_3$, substituted into Equation (1), deformation modulus (E_s) and generalized Poisson's ratio(μ_s) are expressed as follows:

$$\begin{array}{l} \mu_s = \frac{B\sigma_1 - \sigma_3}{\sigma_3(2B-1) - \sigma_3} \\ E_s = \frac{\sigma_1 - 2\mu_s\sigma_3}{\varepsilon_1} \\ B = \frac{\varepsilon_3}{\varepsilon_1} \end{array} \tag{2}$$

where B denotes the ratio of radial strain to axial strain; μ represents the generalized Poisson's ratio; and E is the deformation modulus (GPa).

3.3.1. Deformation Modulus

The deformation modulus of high-temperature sandstone specimens in the whole triaxial unloading confining pressure is calculated by Equation (2), and the curve of deformation modulus changing with confining pressure of high-temperature sandstone specimens under triaxial unloading confining pressure is drawn, as demonstrated in Figure 8.

As shown in Figure 8, with the unloading of confining pressure, the modulus of deformation of the high-temperature sandstone specimen exhibits a trend of overall reduction, and the slope of the curve gradually increases. However, due to the difference in the acting temperature, the modulus of elasticity of the sandstone specimens varies, which is caused by the microcracking of the high-temperature sandstone specimens under the dual action of temperature and unloading, resulting in a sudden drop in stress and a corresponding sudden drop in the modulus of elasticity. As the unloading confining pressure test proceeds, the secondary microcracks emerging within the high-temperature sandstone specimen gradually expand and coalesce, inducing the stress to reverse and increase, and the modulus of elasticity will likewise undergo comparable alterations. Subsequently, it continues to decline in accordance with the original downward tendency. It is apparent that the modulus of elasticity exhibits abrupt reductions followed by recovery behaviors, driven by stress fluctuations during microcrack evolution.

Additionally, it was found that when the high-temperature sandstone specimens were subjected to failure at 25 °C, 200 °C, 400 °C, 600 °C, and 800 °C, their modulus of elasticity were 0.96 GPa, 1.5 GPa, 2.7 GPa, 1.6 GPa, and 0.63 GPa, respectively. Evidently, the modulus of deformation of the sandstone specimen experiencing failure under a constant confining pressure initially rises and subsequently declines with the escalation of the initial acting temperature, with the critical temperature lying between 400 °C and 600 °C.

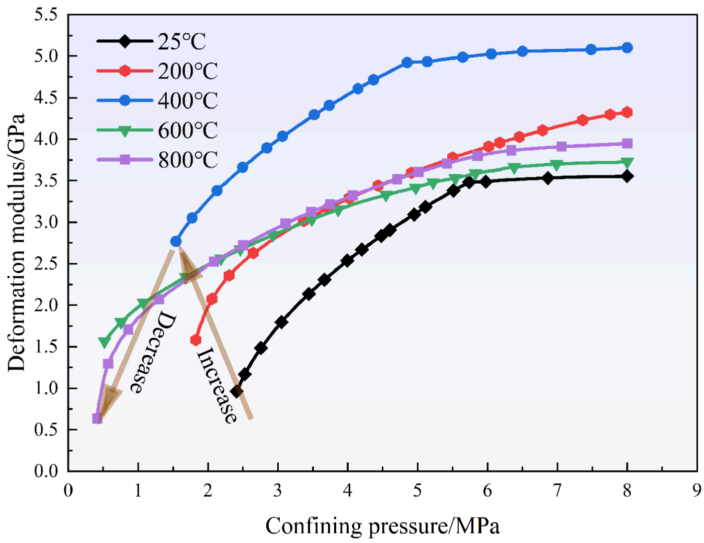

Figure 8. The evolutionary pattern of the deformation modulus of sandstone specimens within the unloading triaxial compression test.

3.3.2. Generalized Poisson's Ratio

Figure 9 shows the variation in the generalized Poisson's ratio of the high-temperature sandstone sample during the unloading stage of the confining pressure. It can be seen from the figure that as the confining pressure decreases during the failure process of the sandstone specimen at 800 °C, the generalized Poisson's ratio of the sandstone specimen is greater than 0.8, indicating that the microcracks generated by the high temperature cause the radial deformation to increase further during unloading, thereby exceeding the Poisson's ratio limit value (0.5) of the elasto-plastic material. It is of note that the generalized Poisson's ratio employed in this unloading confining pressure test is not a material property parameter; rather, it encompasses the volumetric deformation and fracture expansion deformation of the high-temperature sandstone specimen. Additionally, with the elevation of the initial treatment temperature, the generalized Poisson's ratio of the preheated sandstone specimens exhibited an overall upward trend during the failure process. This is because the sandstone specimens would generate initial microcracks under the influence of high temperature. Moreover, during unloading, the microcracks would further propagate along the σ_2 and σ_3 directions under the combined effect of the continuous increase in axial compression and the decrease in confining pressure, thereby giving rise to an increase in the generalized Poisson's ratio.

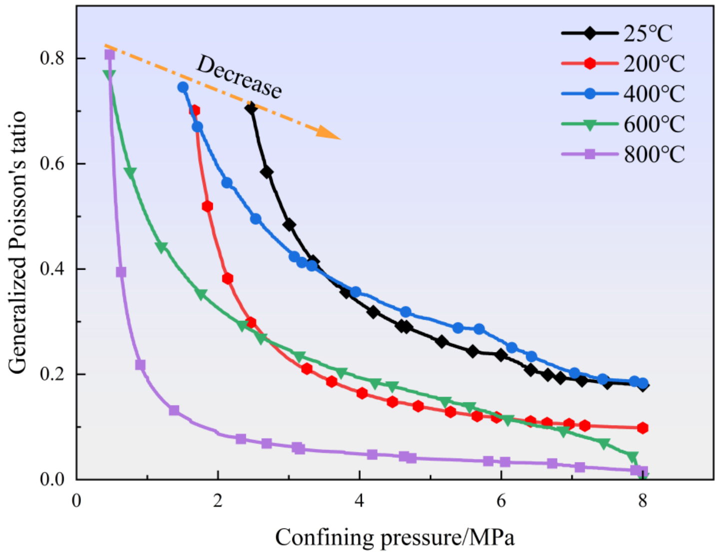

Figure 9. The evolutionary pattern of generalized Poisson's ratio of sandstone specimens within the unloading triaxial compression test.

3.4. Dilatancy Characteristics

The dilatancy behavior of high-temperature sandstone specimens constitutes a common phenomenon where the volume of the test piece undergoes a transformation from compression to expansion under pressure [38–40]. According to the method shown in Figure 10, when the volume of the high-temperature sandstone sample is compressed and then expanded, the sample begins to undergo shear swelling, and the shear swelling stress (σ_{cd}) of the high-temperature sandstone sample is the stress value at the starting point of shear swelling [41,42].

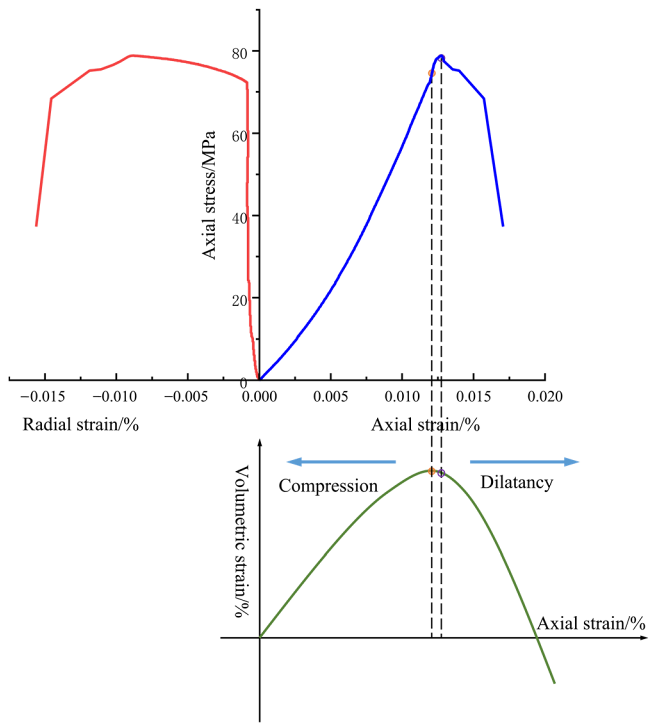

Figure 10. Schematic diagram of dilatancy stress of high-temperature sandstone specimens.

3.4.1. Volume–Axial Strain

Figure 11 shows the volume–axial strain curves of high-temperature sandstone specimens subjected to different temperatures in the triaxial unloading confining pressure test. It can be observed from Figure 11 that the loading curve exhibits a linear growth tendency in the initial phase, with volumetric strain being greater than zero and gradually augmenting. The high-temperature sandstone specimen is in the compression stage. As the unloading confining pressure test persisted, the axial pressure of the high-temperature sandstone sample escalated, whereas the confining pressure initiated to decline, and the curve entered the nonlinear growth phase. The curve grew sluggishly and gradually attained its maximum value (the volume transited from compression to expansion). Subsequently, the curve commences to descend from the point of shear dilation, and the high-temperature sandstone specimen enters the shear dilation stage. As the confining pressure persists in decreasing, the upward tendency of the curve diminishes, signifying that the tensile ductility of the high-temperature sandstone specimen augments under the influence of temperature.

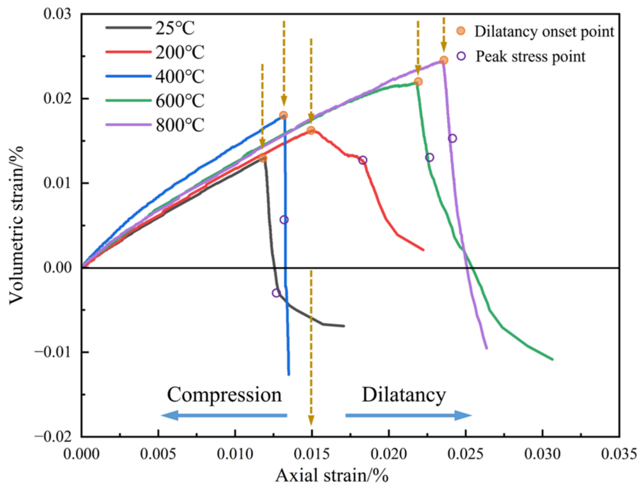

Figure 11. Volume strain–axial strain curve for high-temperature sandstone samples.

In Figure 11, the volumetric strain and axial strain corresponding to the peak stress points are depicted, and it is observable that all the shear dilation stress points occur prior to the peak stress points. The shear dilatancy stress point indicates the transition from compression to expansion of the high-temperature sandstone sample; thus, the volumetric strain corresponding to this shear dilatancy stress point is also the maximum compressive strain of the high-temperature sandstone sample. As the applied temperature rises, the volumetric strain and axial strain at the shear dilation stress position of the sandstone specimen increase, suggesting that the microcracks generated within the sandstone specimen under high-temperature conditions are more likely to undergo further expansion during the axial loading and unloading processes, giving rise to the compressibility of the specimen.

3.4.2. Shear Swelling Stress

Based on the calculation method and the curve results presented in Figures 10 and 11, the evolution law of shear dilatancy stress of high-temperature sandstone specimens at different temperatures is depicted in Figure 12. It can be observed from Figure 12 that the shear dilatancy stress of the sandstone sample shows a gradually increasing trend with the rise in the initial applied temperature. A precise fitting was carried out for the tensile dilatancy stress and temperature of the high-temperature sandstone samples to quantify the relationship between them more accurately. The fitting results are displayed in Figure 12, and the fitting equation is presented by Equation (3).

$$\sigma_{cd} = 71.088 + 0.055\sigma_3 \;\; R^2 = 0.98081 \tag{3}$$

It can be discerned from the fitting results of the equation that the shear dilatancy stress and temperature of the high-temperature sandstone sample demonstrate an excellent linear relationship. Under the same confining pressure, the shear dilatancy stress of the high-temperature sandstone sample rises gradually with the escalation of the acting temperature.

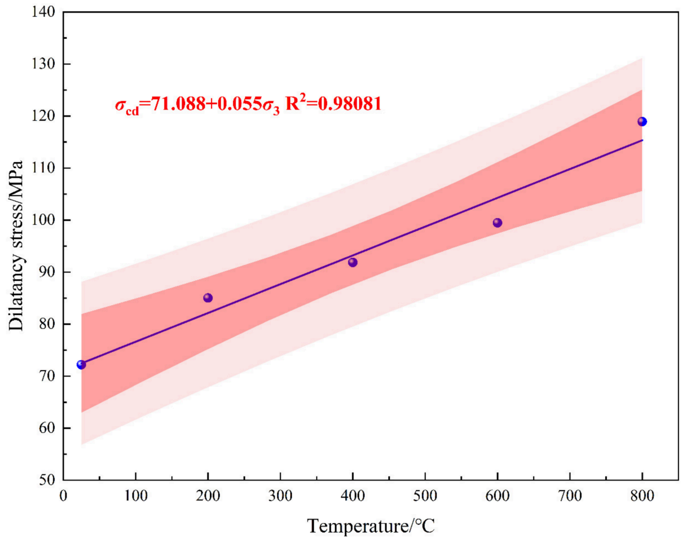

Figure 12. Fitting curve of shear dilation stress–temperature.

Meanwhile, the shear swelling stress and peak stress were also fitted according to the data results in Figure 11, and the relationship between them was determined. The fitting results are shown in Figure 13, and the fitting equation is presented by Equation (4):

$$\sigma_{cd} = -10.164 + 1.037\sigma_c \;\; R^2 = 0.99646 \tag{4}$$

From Figure 13 and Equation (4), it can be seen that there is a good linear relationship between the shear dilatancy stress and peak stress of sandstone specimens under different temperature conditions. The shear dilatancy stress of the high-temperature sandstone specimen likewise exhibited an ascending trend along with the rise in peak stress.

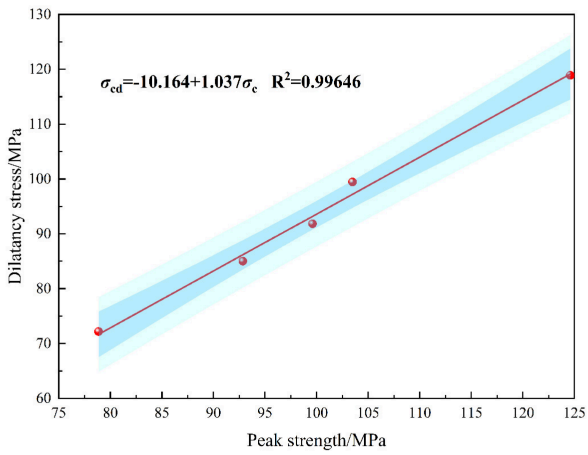

Figure 13. Fitting curve of shear swelling stress–peak stress.

3.4.3. Shear Swelling Level

Commonly, the ratio of the swelling stress to the peak stress (σ_{cd}/σ_c) of high-temperature sandstone is designated as the swelling level. After calculation, the shear swelling level of the high-temperature sandstone sample at 25 °C amounts to 0.9154; that of the sample at 200 °C is 0.9156; at 400 °C, it is 0.9222; at 600 °C, it is 0.9555; and at 800 °C, it is 0.9596. The fitted relationship between the two conforms to an S-shaped exponential pattern, as shown in Figure 14. The analysis suggests that as a consequence of the rise in the acting temperature, the proportion of elastic deformation in the high-temperature sandstone specimen throughout the loading process diminishes, whereas the relative length of the plastic stage elongates and the plasticity augments. During the unloading process, as the thermally treated sandstone undergoes expansion, a shorter duration to reach peak stress leads to a decline in both the peak strength and the associated dilatancy stress, thereby aggravating the degree of shear dilatancy.

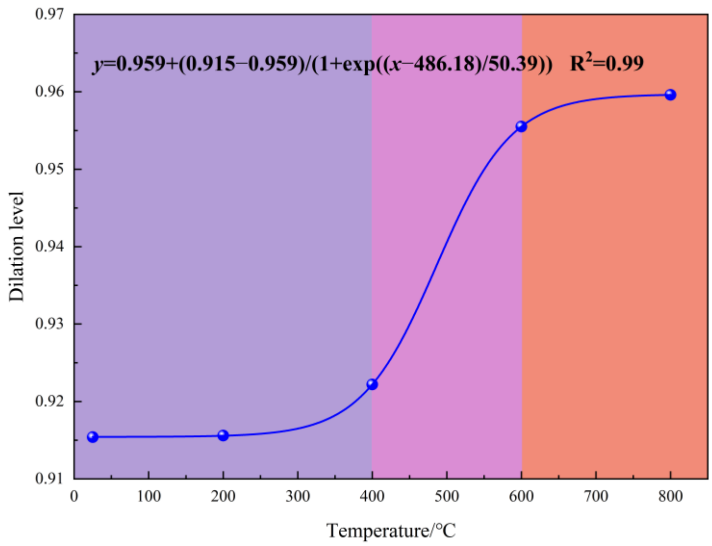

Figure 14. The evolutionary regulation of shear swelling level for high-temperature sandstone samples.

3.4.4. Temperature-Dependent Dilatancy of Sandstone in True Triaxial Compression

The swelling effect pertains to the alteration in the volume characteristics of rocks subsequent to deformation, and the high-temperature sandstone sample will manifest distinct volumetric expansion beneath the unloading path. The shear dilatation angle (ψ) constitutes a physical quantity that delineates the volumetric shear dilatation effect within rocks. Its physical significance lies in the angle between the axial and lateral plastic deformation (ε_{p1} and ε_{p3}) of the deformed rock sample [43]. The value range of the shear dilatation angle is typically $0 \leq \psi \leq \varphi$ (internal friction angle); if $\psi = 0$, the effect of volume dilation is disregarded; if $\psi = \varphi$, the effect of volume dilation is maximized to the fullest extent. According to the literature, the shear swelling angle ψ can be expressed as [42,44,45]:

$$\sin\psi = \frac{d\varepsilon_v^P}{-2d\varepsilon_1^P + d\varepsilon_v^P} \tag{5}$$

where ψ is the shear strain angle (°); $d\varepsilon p1$ is the axial plastic strain differential; and $d\varepsilon_v^P$ is the plastic volumetric strain differential.

In the theory of plastic mechanics, the total strain is the linear superposition of elastic strain and plastic strain ($\varepsilon_i = \varepsilon_{ei} + \varepsilon_{pi}$, i = 1, 2, 3,. . .) and the elastic strain is calculated by Hooke's law. In the event that the elastic modulus E and Poisson's ratio μ of the high-temperature sandstone specimen persist in constancy during the loading and unloading consolidation phases, they can be ascertained from the elastic stage of the test. According to the theory of elasticity, axial elastic strain and plastic strain, as well as volumetric elastic strain and plastic strain, can be expressed as follows:

$$\varepsilon_1^e = \frac{\sigma_1 - 2v\sigma_3}{E} \tag{6}$$

$$\varepsilon_v^e = \frac{(1-2v)\sigma_1 - 2(1-v)\sigma_3}{E} \tag{7}$$

$$\varepsilon_1^p = \varepsilon_1 - \varepsilon_1^e \tag{8}$$

$$\varepsilon_v^p = \varepsilon_v - \varepsilon_v^e \tag{9}$$

The shear expansion angle ψ constitutes a function of the plastic internal variable, and the plastic shear strain $\gamma_p\left(\gamma_p = \varepsilon_1^P - \varepsilon_3^P\right)$ can typically be regarded as the internal variable. To facilitate the comparison of the outcomes of diverse experiments, the stress level at which the sample volume undergoes a transformation from compression to expansion (with the volume strain inflection point σ_{cd} in the true triaxial unloading test) is regarded as the starting point ($\gamma_p = 0$) of the plastic shear strain, while the sample failure point is considered as the end point ($\gamma_p = \gamma_{p\max}$, where $\gamma_{p\max}$ represents the maximum plastic shear strain). Subsequently, it is normalized, and the normalized plastic shear strain $\gamma_{p^*} = \gamma_p/\gamma_{p\max}$ is acquired. The plastic increment can be derived by computing the difference between adjacent (or equally spaced) test data points.

Figure 15 shows the evolution of the shear dilatancy angle of sandstone specimens under different confining pressures during triaxial unconfined compression tests at different temperatures. It can be observed that the evolution pattern of the shear dilatancy angle of sandstone specimens under true triaxial unconfined compression tests at different temperatures remains essentially consistent, that is, the shear dilatancy angle remains stable initially and then increases rapidly and reaches a peak during the unloading process. At a temperature of 25 °C, the maximum value of the shear dilation angle is 71.63°; at 200 °C, it is 76.68°; at 400 °C, it is 85.34°; at 600 °C, it is 86.33°; and at 800 °C, it is 86.87°. The shear dilation angle exhibits an ascending tendency along with the rise in temperature. This is attributed to the thermally induced local defects within the specimen, which promote the development of tensile cracks parallel to the unloading direction under a simultaneous axial loading and confinement unloading path, thereby driving plastic volume expansion. However, the tensile fracture has a smaller effect on axial plastic strain, and the shear–compression action has a smaller effect on axial plastic strain, so the shear swelling angle is larger.

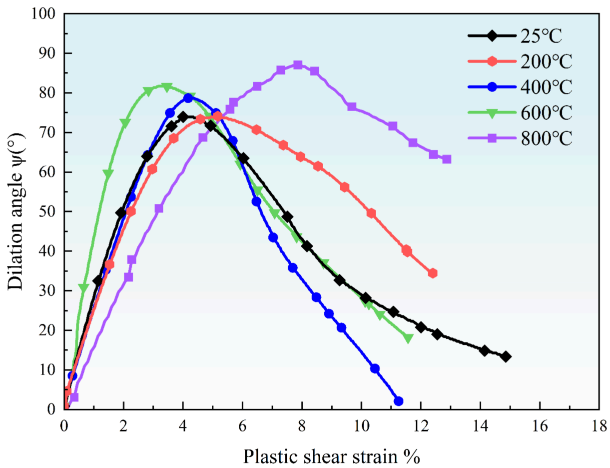

Figure 15. The evolution of shear dilatancy angle in triaxial unconfined compression test of sandstone samples.

The analysis in the previous part discloses that the evolution tendency of the shear swelling angle ψ shows an increase with the rise in temperature. At present, the majority of research has centered on the investigation of the variations in shear swelling under different confining pressures. Nevertheless, the mechanism underlying the evolution of the shear swelling angle under the influence of temperature has not been clarified hitherto. In this section, we endeavor to offer a rational explanation for the evolution behavior of the shear dilation angle under high-temperature circumstances, based on the experiments carried out in the previous section.

Referring back to Reynolds' [46] initial definition, a shear-induced dilation angle was put forward to delineate the relationship between the volume variation and shape alteration of smooth rigid particle media. Considering that the initial supposition when the notion of shear dilation was put forward was that the medium possessed spherical grain shape, uniform grain size, and smooth yet rigid material attributes, it was comparatively straightforward to mathematically deduce the alterations in volume and shape of the material under temperature and loading/unloading operations, and the connection between volume and shape changes could also be quantified geometrically [47]. However, for rock materials, deformation is not only caused by dislocations in mineral grains, but also includes deformation and fracture of minerals. Therefore, the evolution of shear swelling angle should be related to the microscopic fracture of rocks, thus related to the macroscopic failure process of rocks, which has been observed in the author's previous studies [48].

3.4.5. Collective Microscopic Mechanism of the Critical Transition Around 400 °C

The thermo-mechanical behavior of sandstone exhibits a critical transition at 400 °C, governed by the interplay of thermal compaction, mineral degradation, and microcrack evolution. Below this threshold, moisture evaporation and mineral expansion induce thermal compaction that seals initial defects, enhancing peak strength and deformation modulus while restricting unloading-induced failure to localized brittle shear. Conversely, temperatures exceeding 400 °C trigger the desorption of structural bound water and severe anisotropic thermal stresses due to mismatched mineral expansion, generating pervasive intergranular microcracking. Under subsequent true triaxial unloading, this thermal pre-damage facilitates unstable crack propagation, shifting the failure mechanism to a complex tensile–shear multi-fracture mode. This multiscale structural deterioration fundamentally drives the macroscopic anomalies observed beyond 400 °C, notably the deformation modulus reversal, extreme dilatancy, and anomalous volumetric expansion.

3.5. Damage Evolution Characteristics Based on Strain Increment

As shown in Figure 16, under high temperature and external loading, microcracks initiate and propagate from the tips of primary defects within the rock. During their development, secondary cracks interconnect with each other or link up with primary cracks. Primary defects are randomly distributed throughout the specimen with diverse orientations. However, newly formed cracks inevitably propagate along the direction of the maximum principal stress. This propagation leads to surface spalling, radial expansion of the rock sample, and a consequent reduction in the effective bearing area. According to the strain equivalence principle, the deterioration of the specimen's mechanical properties is a consequence of the reduction in effective bearing area, which corresponds to an intensification of damage. Under external loading, cracks initiate within the sandstone, subsequently developing, propagating, and interconnecting. This process results in a diminished effective bearing area and induces damage within the specimen. Accumulation of this damage eventually leads to failure. It is worth noting that secondary cracks develop along the direction of the maximum principal stress under external loading. Concurrent with surface spalling, the sandstone undergoes volumetric expansion.

The rock is partitioned into two distinct regions: the damaged zone and the intact zone, where the damaged zone encompasses both cracks and the solid matrix that has lost its load-bearing capacity; and the intact zone constitutes the effective load-bearing area. Based on the effective load-bearing area concept, the damage variable D is defined as:

$$\left.\begin{array}{r} S = S_e + S_d \\ D = 1 - \frac{S_e}{S} = \frac{S_d}{S} \end{array}\right\} \quad (10)$$

where S is the total cross-sectional area of the specimen; S_e is the effective load-bearing area, referring to the cross-sectional area of the intact zone; S_d is the cross-sectional area of the damaged zone, representing the combined area of cracks and the solid matrix that has lost its load-bearing capacity. As indicated by Equation (10), the damage variable D is defined as the ratio of S_d (damaged zone area) to S (total specimen area). Consequently, the evolution of damage during specimen loading is governed by changes in S_d.

Note that S in Equation (10) is non-constant and differs from the specimen's initial cross-sectional area; instead, S increases during loading as crack proliferation enlarges the void space. Moreover, direct measurement of the damaged zone and intact zone (effective load-bearing area) during loading is experimentally challenging, hindering direct damage assessment via effective load-bearing area evolution. Experimental analysis shows continuous damage accumulation during loading, while crack development drives progressive volumetric expansion of the specimen. Under the assumption that the intact zone's cross-section remains constant at its pre-loading value, changes in total cross-sectional area S arise exclusively from damage zone evolution. Thus, the evolution of damaged zone area S_d is characterizable through specimen volumetric deformation. Leveraging the real-time monitorability of volumetric deformation in true triaxial tests, the damage variable calculation—initially derived from effective load-bearing area—can be reformulated via volumetric deformation evolution.

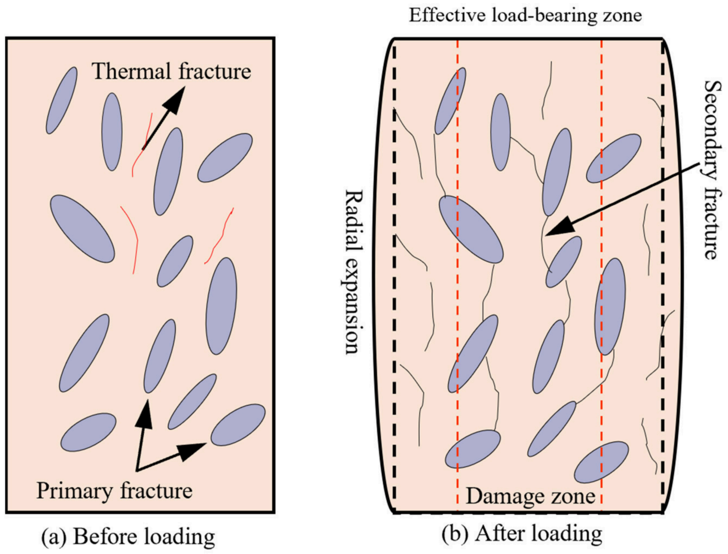

Figure 16. Schematic of progressive failure process in coal specimens under true triaxial compression.

The damage variable D is constrained to [0, 1], where $D = 0$ denotes an intact specimen, and $D = 1$ indicates complete failure with total loss of load-bearing capacity. By normalizing the volumetric deformation evolution and denoting the volumetric strain increment at failure as ε_t, D is defined as:

$$D = \frac{\varepsilon_v}{\varepsilon_t} \tag{11}$$

where ε_v denotes the volumetric strain increment of the specimen throughout the loading process. Critically, all volumetric strain increments are referenced to the initial unloaded state.

As computed by Equation (11), Figure 17 demonstrates immediate damage initiation at the onset of true triaxial loading. During the initial phase, D maintains near-zero values ($D < 0.14$), followed by accelerated escalation in the intermediate phase (Phase II). The final phase (Phase III) exhibits sustained growth with progressive deceleration, signaling damage saturation. Critically, at fixed loading durations, elevated initial temperatures suppress early-stage D in sandstone specimens. This thermo-mechanical response correlates with stress–strain evolution and arises from microstructural modification: thermal dehydration induces crystalline expansion, sealing microcracks and densifying the rock fabric, ultimately enhancing load-bearing capacity.

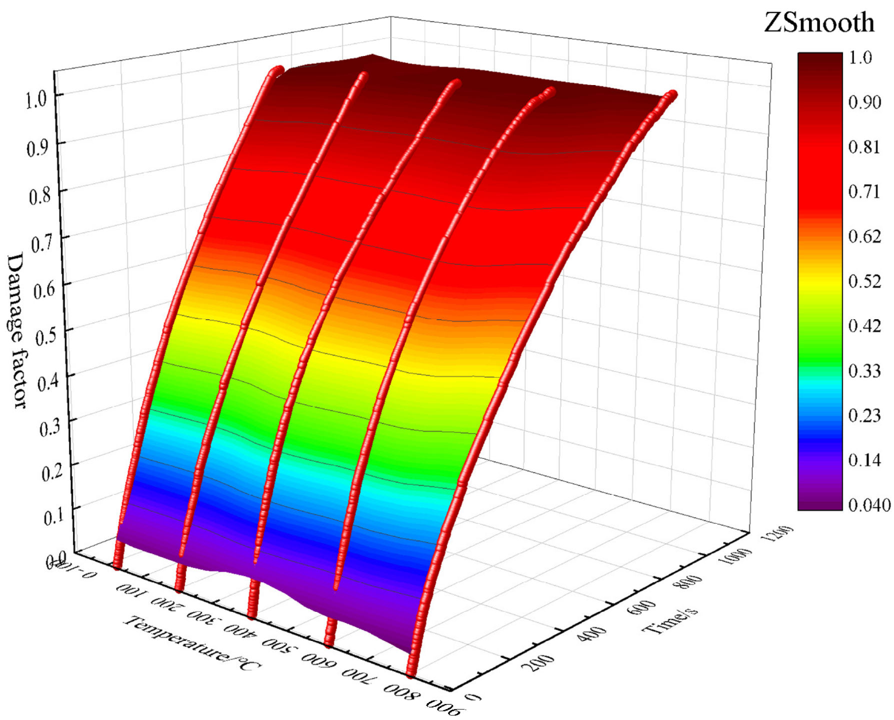

Figure 17. Damage variable evolution in sandstone specimens under true triaxial compression at varied temperatures.

4. Discussion

4.1. Shear–Dilatant Failure Mechanisms in High-Temperature Sandstone Under True Triaxial Compression

Research over the past few decades has yielded a substantial body of experimental evidence on the mechanical behavior of sandstone exposed to high temperatures. Although specimens vary in their mineral composition and grain size, a consensus has emerged on the systematic relationship connecting microscale damage evolution to macroscale mechanical performance. These alterations arise because sandstone, as a multi-mineral aggregate, experiences a range of physicochemical changes under thermal loading (Figure 18a) [49–51]. Under ambient conditions, the initial damage in rock is characterized by the presence of pore water and inherent microcracks [51–53].

https://doi.org/10.3390/app16125979

Upon heating, the macroscopic mechanical response is highly sensitive to the thermal transition temperature (TTT) or a broader thermal transition temperature range (TTTR). Interestingly, some sandstones exhibit a characteristic strengthening effect at mild to elevated temperatures (typically up to 400–500 °C, and in certain highly cemented or porous variants, shifting even higher up to around 600–800 °C) before undergoing severe thermal degradation. In the literature, this strength increase is interpreted through several concurrent and potentially synergistic mechanisms rather than a single process [54–56]. The first and most widely accepted process is that the thermal expansion of mineral grains at relatively low temperatures induces the temporary closure of pre-existing microcracks and pores, which significantly improves the shear resistance of microfractures through the interlocking of grain boundaries. This accommodation of thermal expansion is particularly pronounced in porous sedimentary rocks like sandstones, where a higher initial porosity can mitigate early microstructural thermal damage compared to ultra-compact crystalline rocks. Second, the evaporation and removal of free, absorbed, and structural water can lead to a temporary increase in effective stress, thereby enhancing rock strength. Third, at the intermediate stage, thermally induced microcracks are often isolated and uniformly distributed; when a propagating fissure encounters these isolated microcracks, they can divert the fissure orientation, requiring additional external stress to drive crack advance. Lastly, at higher temperature intervals within this matrix, certain constituent minerals or grain-binding cements may undergo progressive plasticization and localized sintering, which reconnects and crystallizes the contact interfaces between mineral particles, ultimately increasing the intergranular bonding strength [57].

Progression beyond these critical thresholds leads to the accelerated development of irreversible thermal damage, which evolves through two principal mechanisms: (i) the direct generation of new cracks by thermal stress under elevated temperatures or significant thermal gradients, and (ii) interfacial stress concentration resulting from differential thermal expansion among mismatched minerals (e.g., quartz expands significantly more than feldspars), which preferentially weakens grain boundaries and thereby facilitates intergranular crack initiation (Figure 18b). Furthermore, when comparing experimental heating techniques in the literature, works employing variable heating rates (imposing higher gradients for higher target temperatures) often induce more severe early thermal shocks than the more widely used constant heating rate method. However, recent comparative studies indicate that while the heating rate noticeably influences deformability, its effect remains relatively minor compared to the dominant impact of the maximum target temperature itself. Given that the fracture toughness for transgranular propagation generally exceeds that for intergranular paths, cracks are more likely to extend along these thermally weakened grain boundaries under comparable driving forces.

The progression of microscopic damage dictates the macroscale mechanical response. Thermally induced microcracks attenuate the energy threshold required for crack nucleation and growth, thereby expediting the failure process and causing severe strength degradation at extreme temperatures. Concurrently, the development of an extensive crack network modifies the effective stiffness and deformability of the material, which is reflected in a reduced elastic modulus and a more pronounced ductile character of the stress–strain relationship. In sandstone, this threshold interval is heavily influenced by intense thermo-chemical and physical activities, most notably the structural α-β quartz phase transition at approximately 573 °C. This polymorphic transformation induces a sharp increase in unit-cell volume and a critical surge in thermal crack density. The consequent percolation transition within the crack network provides the fundamental mechanism underlying the marked shifts in macroscopic strength and stiffness, driving the transition from quasi-brittle to significantly ductile material behavior.

True triaxial test results indicate that sandstone exhibits accelerated dilatancy with progressive shear displacement prior to failure, manifested as volumetric swelling due to ongoing damage evolution. After the peak stress, sliding along the generated fracture surface occurs, characterized by decreasing roughness and a steady dilation angle, marking the stage of frictional sliding upon crack network percolation. This failure progression is consistent with the gradual failure patterns of sandstone under thermal effects. Both observations jointly validate the damage accumulation trajectory, spanning from the nucleation and growth of microcracks to the development of a macroscopic rupture surface [58–60].

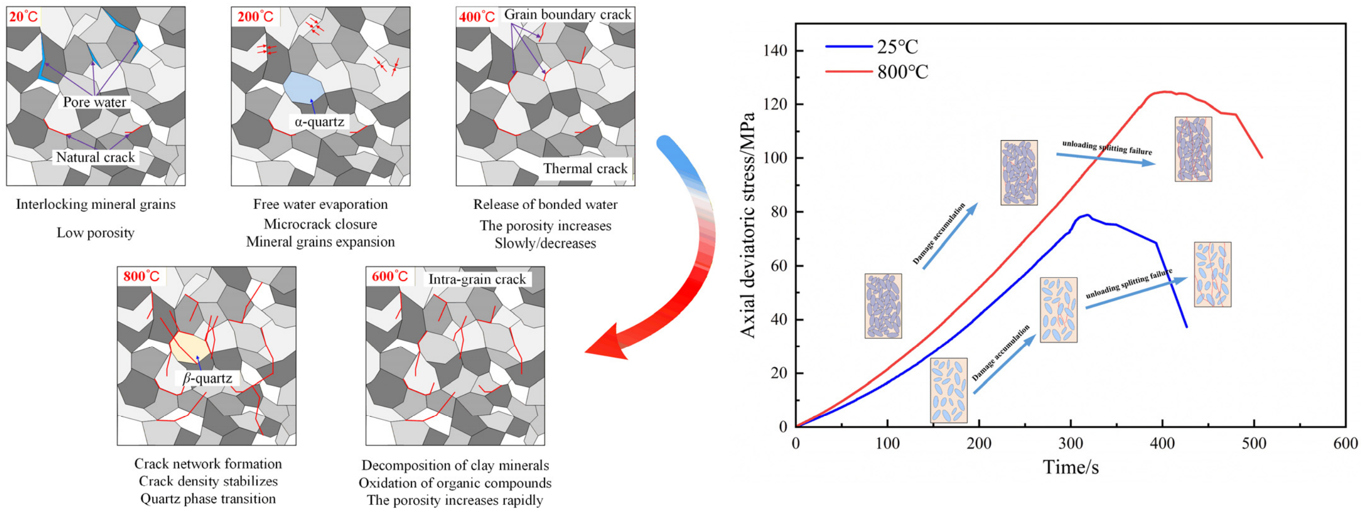

(a) Damage behavior of granite at different temperatures

(b) Stage-dependent variations in mechanical properties with temperature

Figure 18. Damage evolution and fracture mechanisms of granite after high-temperature exposure.

4.2. Engineering Implications of Thermal Damage in Sandstone

The present work demonstrates a systematic evolution in the failure mode of heat-treated sandstone with elevated temperature. At temperatures below 400 °C, the rock displays a "low-temperature strengthening" behavior, wherein failure is predominantly shear-controlled. In the high-temperature regime above 400 °C (particularly ≥600 °C), however, mineral dehydration and widespread microcrack propagation result in a progressive shift towards a combined tensile–shear failure mechanism, with marked occurrence of laminar splitting. This shift suggests that employing the original or low-temperature strength parameters for engineering evaluation would lead to a significant underestimation of collapse risk in high-temperature regions, given the frequently more sudden nature of tensile failure. Thus, a partitioned monitoring strategy is proposed: in high-temperature zones, emphasis should be placed on tensile failure precursors including crack opening displacement and high-frequency acoustic emission events; whereas in low-temperature zones, monitoring may continue to focus primarily on indicators of shear slip.

It is vital to note that the macroscopic failure behaviors and deformation characteristics exhibit strong sensitivity to the testing stress paths and loading/unloading rates. Mechanistically, a lower unloading rate allows more ample duration for subcritical crack growth and time-dependent damage accumulation under the influence of high-temperature histories, which typically intensifies lateral dilatancy and yields lower peak strengths. Moreover, the stress path employed herein (simultaneous σ_1 loading and σ_3 unloading) significantly amplifies the deviatoric stress rate while releasing lateral constraints. Driven by the Poisson effect, this specific path forces the thermally induced microcracks to preferentially propagate and split parallel to the maximum principal stress (σ_1) direction. This macro–microstructural linkage explains why the high-temperature specimens undergo a radical shift from conventional localized single shear failure (typically captured under standard triaxial compression with constant σ_3) to an intricate tensile–shear, layered cleavage destruction mode. This distinct stress-path dependency underscores that simulating the exact unloading state is paramount for accurately evaluating the stability and spalling risks of high-temperature underground gasification cavities. This necessitates a zonally differentiated approach to support design. From a thermodynamic perspective, the high-temperature core region (≥400 °C) requires a composite support system characterized by high prestressing and variable yield resistance to suppress severe dilatancy and interlayer splitting. However, traditional steel rock bolts will inevitably suffer from severe creep, stress relaxation, and thermal expansion mismatches in such extreme temperatures, leading to a substantial decrease in prestressing force. Consequently, the practical implementation of this strategy in underground coal gasification projects requires specialized high-temperature adaptive designs. Incorporating the volumetric strain increment due to dilation as a critical design-check parameter is also recommended. Correspondingly, the monitoring framework must be refined. The integration of acoustic emission parameters and the development of temperature-field-correlated graded warning thresholds will facilitate the early detection of and proactive response to damage progression, thereby improving the long-term operational safety of underground gasification cavities. Incorporating the volumetric strain increment due to dilation as a critical design-check parameter is also recommended. Correspondingly, the monitoring framework must be refined. The integration of acoustic emission parameters and the development of temperature-field-correlated graded warning thresholds will facilitate the early detection of and proactive response to damage progression, thereby improving the long-term operational safety of underground gasification cavities, as shown in Figure 19.

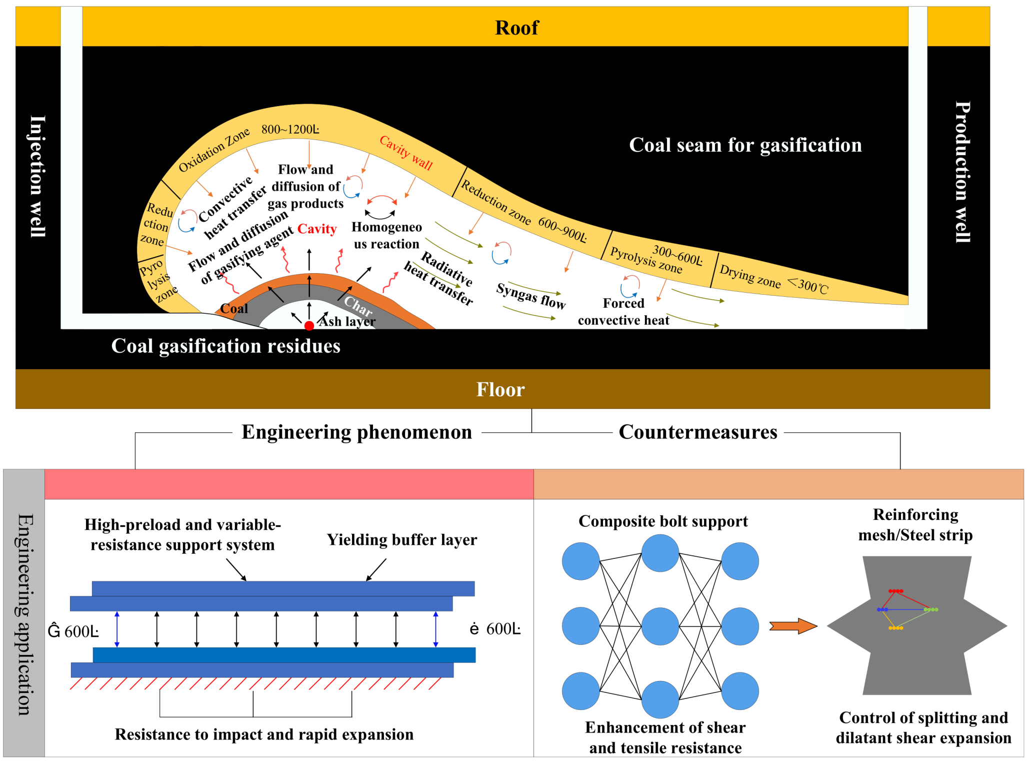

Figure 19. Process of underground coal gasification and corresponding support strategy.

5. Conclusions

This study systematically investigates the evolution of multiscale mechanical behavior and damage mechanisms in sandstone under coupled temperature and stress path conditions through true triaxial loading–unloading tests after high-temperature exposure. The main findings are summarized as follows:

(1) The influence of high temperature on the strength and deformation behavior of sandstone exhibits stage-specific characteristics. The peak strength of sandstone increases nonlinearly with rising temperature. At 800 °C, the strength under loading and unloading paths increased by 67% and 43%, respectively, compared to that at room temperature (25 °C). Beyond 400 °C, the post-peak stress–strain curves display notable ductile features and secondary peak phenomena, indicating a transition from brittle to ductile failure modes.

(2) The failure mode of sandstone is governed by temperature and exhibits a distinct mechanism transition threshold. At temperatures below 400 °C, failure is predominantly characterized by typical V-shaped shear. When the temperature exceeds 400 °C (especially $\geq$600 °C), the failure mechanism shifts to a tensile–shear composite type, accompanied by significant bedding splitting. The failure angle increases continuously with temperature, and the unloading failure angle (up to 81°) consistently exceeds the triaxial compression failure angle at the same temperature.

(3) A quantitative thermal damage characterization method based on the generalized Poisson's ratio and volumetric strain increment is proposed. At 800 °C under unloading failure, the generalized Poisson's ratio of sandstone exceeds 0.8, far surpassing the conventional elastic–plastic material limit of 0.5, demonstrating high sensitivity to thermally induced microcrack propagation. A damage variable D evolution model, defined by the normalized volumetric strain increment ($\varepsilon_v/\varepsilon_t$), is established, enabling quantitative description of the three-stage damage process: "slow accumulation–accelerated development–tending toward saturation".

(4) The evolution of dilatancy characteristics in sandstone under temperature effects is revealed. The dilatancy stress, dilatancy level, and dilation angle all increase monotonically with temperature. Specifically, the dilation angle rises from 71.63° at 25 °C to 86.87° at 800 °C. The dilatancy stress (σ_{cd}) shows a strong linear correlation with both temperature (T) and peak strength (σ_c). This indicates that the enhanced intergranular frictional resistance at elevated temperature is the fundamental cause of intensified dilatancy.

(5) The study provides a design basis for stability control in underground coal gasification engineering. The temperature dependence of strength and failure modes suggests that using room-temperature parameters would significantly underestimate instability risks in high-temperature zones. Based on the 400 °C threshold, a zoned support and monitoring strategy is proposed: support in the high-temperature core zone ($\geq$400 °C) should feature "high pre-tightening force + adaptable resistance" to cope with strong tensile–shear failure, with emphasis on monitoring crack opening displacement and high-frequency acoustic emission events. In contrast, traditional shear-oriented designs remain applicable in low-temperature zones.

Author Contributions: J.L.: Writing—original draft, formal analysis, data curation, conceptualization. B.C.: Writing—review and editing, methodology, funding acquisition. Y.L.: Writing—review and editing, validation. J.M. (Jian Ma): Investigation, data curation, funding acquisition. C.Y.: Methodology, conceptualization, funding acquisition. J.M. (Jingong Ma): Resources, project administration, funding acquisition. Z.X.: Supervision. All authors have read and agreed to the published version of the manuscript.

Funding: This research was sponsored by the Deep Earth Probe and Mineral Resources Exploration-National Science and Technology Major Project (2024ZD1004100, 2024ZD1004105); Xizang Autonomous Region Science and Technology Plan Project (XZ202501ZY0108); Basic Research Program of Jiangsu (Grant No. BK20240431); Shanxi provincial basic research program (202303021211260); Qing Lan Project of JiangSu Province and the Zhangjiagang Science and Technology Development Plan of Zhangjiagang Science and Technology Bureau (Grant No. ZKHB2439).

Institutional Review Board Statement: Not applicable.

Informed Consent Statement: Not applicable.

Data Availability Statement: The raw data supporting the conclusions of this article will be made available by the authors on request.

Conflicts of Interest: Author Jingong Ma was employed by the company China Coal Technology & Engineering Group Taiyuan Research Institute Co. The remaining authors declare that the re-search was con-ducted in the absence of any commercial or financial relationships that could be construed as a po-tential conflict of interest.

References

1. Green, M. Recent developments and current position of underground coal gasification. *Proc. Inst. Mech. Eng. Part A-J. Power Energy* **2018**, *232*, 39–46. [CrossRef]
2. Maugh, T.H., 2nd. Underground gasification: An alternate way to exploit coal. *Science* **1977**, *198*, 1132–1134. [CrossRef]
3. Zhao, J.; Guo, Y.; Chen, P.; Hu, L.; Wang, J. True Triaxial Shear Strength and Failure Mechanism of Sandstone Under Real-Time High-Temperature Conditions. *Rock Mech. Rock Eng.* **2025**, *58*, 6211–6231. [CrossRef]
4. Liu, S.; Xu, J. Analysis on damage mechanical characteristics of marble exposed to high temperature. *Int. J. Damage Mech.* **2015**, *24*, 1180–1193. [CrossRef]
5. Liu, L.; Jin, J.; Liu, J.; Cheng, W.; Zhao, M.; Luo, S.; Luo, Y.; Wang, T. Mechanical properties of sandstone under in-situ high-temperature and confinement conditions. *Int. J. Miner. Metall. Mater.* **2025**, *32*, 778–787. [CrossRef]
6. Takyi, S.A.; Zhang, Y.; Si, M.; Zeng, F.; Li, Y.; Tontiwachwuthikul, P. Current status and technology development in implementing low carbon emission energy on underground coal gasification (UCG). *Front. Energy Res.* **2023**, *10*, 1051417. [CrossRef]
7. Mandal, R.; Maity, T. Operational process parameters of underground coal gasification technique and its control. *J. Process Control* **2023**, *129*, 103031. [CrossRef]
8. Tomás, R.; Benavente, D.; Martínez-Ibáñez, V.; Garrido, M.E. How do high temperatures affect rock properties? A comprehensive review of experimental thermal effects and underlying mechanisms. *Eng. Geol.* **2025**, *357*, 108323. [CrossRef]
9. Wang, P.; Deng, J.; Liu, W.; Xiao, Q.; Lv, Q.; Zhang, Y.; Hou, Y. Thermo-Mechanical Numerical Analysis of strain and Damage Distribution within the Surrounding Rock of Underground Coal Gasification Panels. *Processes* **2023**, *11*, 2521. [CrossRef]
10. Jowkar, A.; Sereshki, F.; Najafi, M. A new model for evaluation of cavity shape and volume during Underground Coal Gasification process. *Energy* **2018**, *148*, 756–765. [CrossRef]
11. Yang, L. Coal properties and system operating parameters for underground coal gasification. *Energy Sources Part A-Recovery Util. Environ. Eff.* **2008**, *30*, 516–528. [CrossRef]
12. Qin, W.; Zhao, Y.; Jin, A.; Chen, S.; Liu, J. Analysis of precursor and failure mechanisms of granite under high temperature: Based on acoustic emission and 3D-DIC perspectives. *Constr. Build. Mater.* **2025**, *473*, 141049. [CrossRef]
13. Gautam, P.K.; Verma, A.K.; Sharma, P.; Singh, T.N. Evolution of Thermal Damage Threshold of Jalore Granite. *Rock Mech. Rock Eng.* **2018**, *51*, 2949–2956. [CrossRef]
14. Zhang, Y.; Wan, Z.; McLennan, J.; Gu, B.; Ta, X. Influence of Temperature on Physical and Mechanical Properties of a Sedimentary Rock Coal Measure Mudstone. *Therm. Sci.* **2021**, *25*, 159–169. [CrossRef]
15. Gu, B.; Wan, Z.; Zhang, Y.; Ma, Y.; Xu, X.B. Influence of Real-Time Heating on Mechanical Behaviours of Rocks. *Adv. Civ. Eng.* **2020**, *2020*, 8879922. [CrossRef]
16. Zhao, Y.; Wan, Z.; Feng, Z.; Yang, D.; Zhang, Y.; Qu, F. Triaxial compression system for rock testing under high temperature and high pressure. *Int. J. Rock Mech. Min. Sci.* **2012**, *52*, 132–138. [CrossRef]
17. Liu, Z.; Wang, C.; Zhou, H.; Shen, W.; Shao, J. A true triaxial time-dependent test system with two rigid and one flexible loading frame for rock under real-time high temperature and high pressure and its application. *Chin. J. Geotech. Eng.* **2021**, *40*, 2477–2486.
18. Shi, X.; Jing, H.; Yin, Q.; Zhao, Z.; Han, G.; Gao, Y. Investigation on physical and mechanical properties of bedded sandstone after high-temperature exposure. *Bull. Eng. Geol. Environ.* **2020**, *79*, 2591–2606. [CrossRef]
19. Su, H.; Jing, H.; Yin, Q.; Yu, L.; Wang, Y.; Wu, X. Strength and deformation behaviors of veined marble specimens after vacuum heat treatment under conventional triaxial compression. *Acta Mech. Sin.* **2017**, *33*, 886–898. [CrossRef]
20. Wang, G.; Zheng, J.; Liu, Y.; Qing, Z.; Yang, B.; Fan, Y. Study on the evolution law of true triaxial unloading mechanical properties of sandstone after high temperature. *Coal Sci. Technol.* **2024**, *6*, 1–16.

21. Ma, X.; Ma, D.; Hu, D.; Zhou, H.; Chen, S.; Yu, Z.; Tan, X. A real-time high-temperature true triaxial test system and its application. *Chin. J. Rock Mech. Eng.* **2019**, *38*, 1605–1614.
22. Wagner, H. Deep Mining: A Rock Engineering Challenge. *Rock Mech. Rock Eng.* **2019**, *52*, 1417–1446. [CrossRef]
23. He, M.; Wang, Q. Rock dynamics in deep mining. *Int. J. Min. Sci. Technol.* **2023**, *33*, 1065–1082. [CrossRef]
24. Bukowska, M. Post-peak failure modulus in problems of mining geo-mechanics. *J. Min. Sci.* **2013**, *49*, 731–740. [CrossRef]
25. Wei, J.; Liao, H.; Liang, H.; Li, N.; Gao, F.; Zhang, D. Investigation on dynamic mechanical behaviors and energy consumption of conglomerate under three-dimensional static stress. *J. China Univ. Pet. (Ed. Nat. Sci.)* **2024**, *47*, 102–110.
26. Wei, J.; Liao, H.; Wang, H.; Chen, J.; Li, N.; Zhang, D. Experiment on mechanical properties of conglomerate rocks under true triaxial loading. *J. China Univ. Pet. (Ed. Nat. Sci.)* **2022**, *46*, 81–89.
27. Li, Z. Study on Mechanical Properties and Failure Mechanism of Rock Under True Triaxial Loading and Unloading Conditions. Ph.D. Thesis, University of Mining and Technology, Xuzhou, China, 2019.
28. Li, Z.; Zhou, W.; Wang, L.; Li, W.; Tian, Y.; Zhang, C. Unloading properties and fracture characteristics of rock under different true triaxial unloading paths. *J. Min. Saf. Eng.* **2022**, *39*, 480–488.
29. Ma, T.; Ma, D.; Yang, Y. Fractal Characteristics of Coal and Sandstone Failure under Different Unloading Confining Pressure Tests. *Adv. Mater. Sci. Eng.* **2020**, *2020*, 2185492. [CrossRef]
30. Yang, R.; Ma, D.; Yang, Y. Experimental Investigation of Energy Evolution in Sandstone Failure during Triaxial Unloading Confining Pressure Tests. *Adv. Civ. Eng.* **2019**, *2019*, 7419752. [CrossRef]
31. Ma, P.; Zhou, Y.; Liu, C.; Shang, Y. Energy evolution characteristics of coal failure in triaxial tests under different unloading confining pressure rates. *Rock Soil Mech.* **2019**, *40*, 8.
32. Zhou, X.; Zhang, Y.; Ha, Q. Real-time computerized tomography (CT) experiments on limestone damage evolution during unloading. *Theor. Appl. Fract. Mech.* **2008**, *50*, 49–56. [CrossRef]
33. Haimson, B.C.; Chang, C. True triaxial strength of the KTB amphibolite under borehole wall conditions and its use to estimate the maximum horizontal in situ stress. *J. Geophys. Res. Solid Earth* **2002**, *107*, ETG 15-11–ETG 15-14. [CrossRef]
34. Trzeciak, M.; Sone, H. Critical review of the Mogi failure criterion based on true-triaxial laboratory data analysis and theoretical considerations. *Int. J. Rock Mech. Min. Sci.* **2022**, *159*, 105220. [CrossRef]
35. Al-Ajmi, A.M.; Zimmerman, R.W. Stability analysis of vertical boreholes using the Mogi–Coulomb failure criterion. *Int. J. Rock Mech. Min. Sci.* **2006**, *43*, 1200–1211. [CrossRef]
36. Gao, C.-Y.; Xu, J.; He, P.; Liu, J.-F. Study on mechanical properties of marble under loading and unloading conditions. *Yanshilixue Yu Gongcheng Xuebao/Chin. J. Rock Mech. Eng.* **2005**, *24*, 456–460.
37. Zhu, Z.; Yu, L.; Li, J.; Meng, Q.; Sui, B.; Zhang, Z. Deformation evolution and dissipated energy characteristics of marble under pre-peak unloading conditions. *J. China Coal Soc.* **2020**, *45*, 181–190.
38. Wang, Y.; Wu, J.; Pu, H. Effect of calcium formate as an accelerator on dilatancy deformation, strength and microstructure of cemented tailings backfill. *Chemosphere* **2022**, *291*, 132710. [CrossRef]
39. Wu, J.; Feng, M.; Mao, X.; Xu, J.; Zhang, W.; Ni, X.; Han, G. Particle size distribution of aggregate effects on mechanical and structural properties of cemented rockfill: Experiments and modeling. *Constr. Build. Mater.* **2018**, *193*, 295–311. [CrossRef]
40. Wang, Y.; Wu, J.; Ma, D.; Yang, S.; Yin, Q.; Feng, Y. Effect of aggregate size distribution and confining pressure on mechanical property and microstructure of cemented gangue backfill materials. *Adv. Powder Technol.* **2022**, *33*, 103686. [CrossRef]
41. Liu, W.; Hu, Z.; Liu, C.; Huang, X.; Hou, J. Mechanical properties under triaxial compression of coal gangue-fly ash cemented backfill after cured at different temperatures. *Constr. Build. Mater.* **2024**, *411*, 134268. [CrossRef]
42. Zhao, R.; Li, C. A new dilation angle model for rocks. *Rock Mech. Rock Eng.* **2022**, *55*, 5345–5354. [CrossRef]
43. Alejano, L.; Alonso, E. Considerations of the dilatancy angle in rocks and rock masses. *Int. J. Rock Mech. Min. Sci.* **2005**, *42*, 481–507.
44. Chen, Y.; Ma, L.; Fan, P.; Yang, X.; Dong, L. Nonlinear volumetric deformation behavior of rock salt using the concept of mobilized dilatancy angle. *Open Civ. Eng. J.* **2016**, *10*.. [CrossRef]
45. Cook, N. An experiment proving that dilatancy is a pervasive volumetric property of brittle rock loaded to failure. *Rock Mech.* **1970**, *2*, 181–188.
46. Reynolds, O. LVII. On the dilatancy of media composed of rigid particles in contact. With experimental illustrations. *Lond. Edinb. Dublin Philos. Mag. J. Sci.* **1885**, *20*, 469–481. [CrossRef]
47. Barton, N. The shear strength of rock and rock joints. In *International Journal of Rock Mechanics and Mining Sciences & Geomechanics Abstracts*; Pergamon: Oxford, UK, 1976; pp. 255–279.
48. Zheng, Z.-Q.; Liu, H.-Z.; Zhuo, L.; Xiao, M.-L.; Xie, H.-Q.; He, J.-D.; Peng, M.-L. Experimental study on the dilatancy and energy evolution behaviors of red-bed rocks under unloading conditions. *Materials* **2023**, *16*, 5759. [CrossRef]
49. Tang, Y.; Ranjith, P. An experimental and analytical study of the effects of shear displacement, fluid type, joint roughness, shear strength, friction angle and dilation angle on proppant embedment development in tight gas sandstone reservoirs. *Int. J. Rock Mech. Min. Sci.* **2018**, *107*, 94–109. [CrossRef]

50. Ge, Y.; Tang, H.; Ez Eldin, M.; Wang, L.; Wu, Q.; Xiong, C. Evolution process of natural rock joint roughness during direct shear tests. *Int. J. Geomech.* **2017**, *17*, E4016013.
51. Sanei, M.; Faramarzi, L.; Fahimifar, A.; Goli, S.; Mehinrad, A.; Rahmati, A. Shear strength of discontinuities in sedimentary rock masses based on direct shear tests. *Int. J. Rock Mech. Min. Sci.* **2015**, *75*, 119–131. [CrossRef]
52. Han, G.; Zhou, H.; Hou, J.; Zhang, C.; Singh, H.K.; Gao, Y. A comprehensive investigation on the shear properties of interlayer shear weakness zones. *Bull. Eng. Geol. Environ.* **2021**, *80*, 8765–8787. [CrossRef]
53. Andreotti, G.; Graziotti, F.; Magenes, G. Expansion of mortar joints in direct shear tests of masonry samples: Implications on shear strength and experimental characterization of dilatancy. *Mater. Struct.* **2019**, *52*, 64. [CrossRef]
54. Dong, Z.; Chen, Y.; Wang, X.; Kong, L.; Wang, L.; Li, X.; Sun, F.; Ding, K.; Wu, H.; Chen, S.; et al. Evaluation of Thermophysical and Mechanical Properties of Sandstone Due to High-Temperature. *Materials* **2022**, *15*, 8692. [CrossRef]
55. Sun, H.; Sun, Q.; Deng, W.; Zhang, W.; Lu, C. Temperature effect on microstructure and P-wave propagation in Linyi sandstone. *Appl. Therm. Eng.* **2017**, *115*, 913–922. [CrossRef]
56. Gao, Z.; Liu, Z.; Tian, F.; Shen, W. Strength, energy evolution and cracking process of sandstone under high-temperature and high-pressure coupled true triaxial compression. *Geomech. Geophys. Geo-Energy Geo-Resour.* **2022**, *8*, 176. [CrossRef]
57. Li, Q.; Yin, T.; Li, X.; Zhang, S. Effects of rapid cooling treatment on heated sandstone: A comparison between water and liquid nitrogen cooling. *Bull. Eng. Geol. Environ.* **2020**, *79*, 313–327. [CrossRef]
58. Cantieni, L.; Anagnostou, G. The effect of the stress path on squeezing behavior in tunneling. *Rock Mech. Rock Eng.* **2009**, *42*, 289–318. [CrossRef]
59. Huang, X.; Liu, Q.-S.; Bo, Y.; Liu, B.; Ding, Z.-W.; Zhang, Q.-T. An elasto-plastic and viscoplastic damage constitutive model for dilatancy and fracturing behavior of soft rock squeezing deformation. *J. Mt. Sci.* **2022**, *19*, 826–848. [CrossRef]
60. Li, B.; Ding, Q.-F.; Xu, N.-W.; Dai, F.; Xu, Y.; Qu, H.-L. Characteristics of microseismic b-value associated with rock mass large deformation in underground powerhouse caverns at different stress levels. *J. Cent. South Univ.* **2022**, *29*, 693–711. [CrossRef]